DEIReconstructor: a software for diffraction enhanced imaging processing and tomography reconstruction*

ZHANG Kai(张凯)[1] YUAN Qing-Xi(袁清习)[1] HUANG Wan-Xia(黄万霞)[1]
ZHU Pei-Ping(朱佩平)[1,2)] WU Zi-Yu(吴自玉)[1,2,1)]

[1] Institute of High Energy Physics, Chinese Academy of Science, Beijing 100049, China
[2] National Synchrotron Radiation Laboratory, University of Science and Technology of China, Hefei 230026, China

Abstract: Diffraction enhanced imaging (DEI) has been widely applied in many fields, especially when imaging low-Z samples or when the difference in the attenuation coefficient between different regions in the sample is too small to be detected. Recent developments of this technique have presented a need for a new software package for data analysis. Here, the Diffraction Enhanced Image Reconstructor (DEIReconstructor), developed in Matlab, is presented. DEIReconstructor has a user-friendly graphical user interface and runs under any of the 32-bit or 64-bit Microsoft Windows operating systems including XP and Win7. Many of its features are integrated to support imaging preprocessing, extract absorption, refractive and scattering information of diffraction enhanced imaging and allow for parallel-beam tomography reconstruction for DEI-CT. Furthermore, many other useful functions are also implemented in order to simplify the data analysis and the presentation of results. The compiled software package is freely available.

Key words: X-ray imaging, computed tomography, synchrotron radiation source, image processing

PACS: 87.59.-e, 81.70.Tx, 07.85.Qe **DOI:** 10.1088/1674-1137/38/10/106202

1 Introduction

During the past 10 years, various phase-sensitive imaging methods have been developed, because the X-ray phase shift in the kiloelectronvolt energy range can be 1000 times greater than the X-ray attenuation [1, 2]. The diffraction enhanced imaging (DEI) method, known as one of the main phase contrast imaging methods [3, 4], is characterized by extraordinary image quality and greatly enhanced contrast, and is a very promising method capable of enhancing the spatial resolution and allowing features inside an object to be resolved. Combining this imaging technology with the computerized tomography (CT) theory, Dilmanian et al. first extended DEI to the CT mode at NSLS in 2000 [1]. Since then, DEI-CT methods have been widely used for visualizing the morphology of samples, and for assessing quantitative information on their three-dimensional (3D) geometries and properties. Much relevant research has been performed, such as that of Pavlov et al. [5] and Zhu et al. [6–8]. However, quite often difficulties arise when performing DEI experiments. For example, X-ray imaging detectors are sensitive to intensity modulations only. The phase information, however, is also embedded in the recorded images; this information cannot be accessed directly, but requires post-processing procedures to extract the absorption, refraction and scattering information, which is a daunting and protracted undertaking for non-professionals. Furthermore, recent progress in detector development tends to decrease the pixel size while increasing the pixel number. As a consequence, a large number of DEI-CT projections are required for existing CT algorithms to generate reconstructions without significant artifacts. Subsequently the amount of DEI-CT data has increased accordingly, sometimes exceeding several gigabytes. Tomographic data reconstruction is therefore a heavy computing task and a critical issue for DEI-CT experiments [9].

In order to overcome the above difficulties, and to meet the specific needs of the experiments at the 4W1A beamline at the Beijing Synchrotron Radiation Facility (BSRF), we have developed the DEIReconstructor software package to meet the demands of modern DEI experiments. The DEIReconstructor software package, shown

Received 15 November 2013, Revised 26 March 2014

∗ Supported by National Basic Research Program of China (2012CB825800), National Natural Science Foundation of China (11205189, 11375225, 81271574, U1332109) and Knowledge Innovation Program of Chinese Academy of Sciences (KJCX2-YW-N42)

1) E-mail: wuzy@ustc.edu.cn

2) E-mail: zhupp@ihep.ac.cn

in Fig. 1, presents the synchrotron radiation community with a flexible, unified, and reliable graphical user interface (GUI), which integrates mathematical and visualization capabilities to simplify image processing, reconstruction and analysis. In this paper, we present the principles and some examples of the three main features available within the DEIReconstructor software package. These are: (i) data processing, i.e. image processing programs for flat field and dark field correction, normalization, and rotation center determination; (ii) DEI-CT reconstruction, a program to reconstruct the distribution of the decrement of the refractive index, the absorption index and the gradient of the refractive index in the sample; and (iii) DEI information extraction, a program to extract the sample's absorption, refraction and scatter information from DEI. Options for performing parallel computing have been implemented in most of these features in order to make full use of multiple-core processors where available. At the time of writing, the DEIReconstructor software has been used by the beam line experimentalists at BSRF.

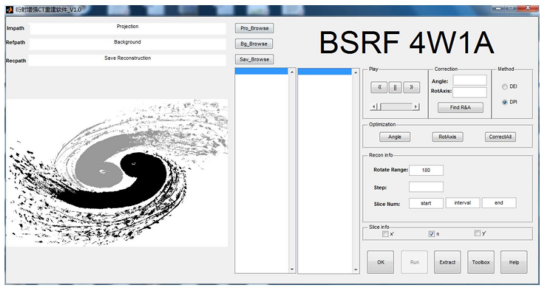

Fig. 1. The DEIreconstructor GUI.

2 Features of data processing

DEI-CT has had a revolutionary impact on medical diagnosis and also has been successfully used in industrial non-destructive testing. However, there are many other factors that introduce significant artifacts in the raw images, such as uneven illumination, lighting variation, noise and instrumentation misalignment. Therefore, pre-processing the DEI projective image is required before reconstruction. The correction and optimization menus shown in Fig. 1 provide flat-field and dark-field correction, rotation center determination, and normalization to calibrate these artifacts. All these preprocessing features will be explained in the following.

As shown in Fig. 2, the calibration process for DEI data is divided into three steps. The first step is flat-field and dark field correction. In the practical case of a DEI-CT experiment, the X-ray doesn't illuminate the CCD homogeneously. Scratches and contamination on optical surfaces also leads to further shadowing of detector areas. Moreover, non-uniform responses of the scintillator and CCD detector will always add noise to the raw images. All these features will reduce the image quality and the ability to obtain accurate images from the digital output of a CCD, so the corrections are necessary. The process by which a CCD detector is corrected is known as flat-field and dark field correction, and can be described by the following equation:

$$I_{\rm pc}=\frac{I_{\rm projective}-I_{\rm dark}}{I_{\rm flat}-I_{\rm dark}} \tag{1}$$

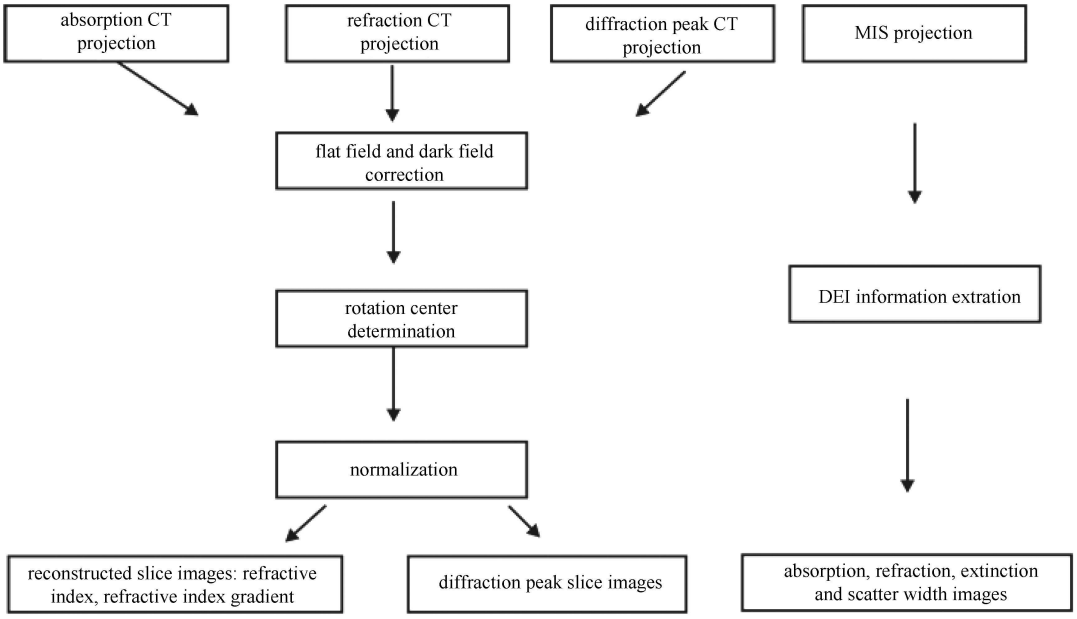

Fig. 2. DEIreconstructor software workflow.

where $I_{\rm pc}$ is the calibrated image and $I_{\rm projective}$ is the raw image. $I_{\rm flat}$ is the image which is measured with the X-rays on, but without a sample in the beam, and is an image which is collected in the absence of any X-rays, and includes both dark current and the bias. Dark current is the thermal noise generated within the CCD and is proportional to a power law of the CCD temperature, while the bias within an image results from an intentional signal introduced to ensure negative values are not processed in the analogue to digital conversion. Both these effects should be corrected by subtraction of the dark field image. After corrections using Eq. (1), a projective image with reduced artifacts and improved quality can be achieved, but during this process, Eq. (1) may create extreme values when $I_{\rm flat}-I_{\rm dark}$ is equal to zero. This is problematic when extracting refraction or absorption information or doing the reconstruction in a DEI-CT experiment. In the DEIReconstructor, it is set to zero if the resulting value was negative. This solves the problem without affecting the accuracy of refraction or absorption information extraction, and also allows accurate image reconstruction.

After the flat-field and dark field correction, the rotation center determination is needed to locate the CT rotation axis in the image center. In the ideal case, the DEI-CT system can be considered as a parallel beam CT system, where the reconstruction algorithm assumes that the rotation axis should be parallel to the detector and is projected onto the central column of the detector shown in Fig. 3(a). In practice, however, it is impossible to accurately avoid any geometric misalignment in the DEI-CT system. Even a small error in the estimation of any parameter can cause visibly detrimental effects on the reconstructed image. Therefore, it is necessary to accomplish the rotation center determination before CT reconstruction. The DEIReconstructor uses the relative spatial position between the axis of rotation and the central column of the detector to describe the geometric misalignment of the whole DEI-CT system shown in Fig. 3(b), and the estimation value of two parameters-angle offset $\Delta\theta$ and displacement offset Δz will be calculated to calibrate the projective image collected by the DEI-CT system. The procedure is follows: firstly, several pairs of mirror symmetric feature points are extracted from the projective images collected at 0 and 180 degrees; secondly, each pair is connected to find the center points, then the center points are connected using the straight line equation fitted by the least square curved-fitting method; this is then used as the rotation axis. If the rotation axis and the central column of the detector cross, the angle between them is the angle offset, and the horizontal distance between these two straight lines is the displacement offset. Finally, based on these two parameters, angle offset and displacement offset, the projective image is rotated and shifted horizontally to make the rotation axis and the central column of the detector coincide with each other. Using the above calibration, the reconstruction results are improved. Moreover, using the optimization menu shown in Fig. 1, the user can further refine the rotation center manually by verifying the resulting slices.

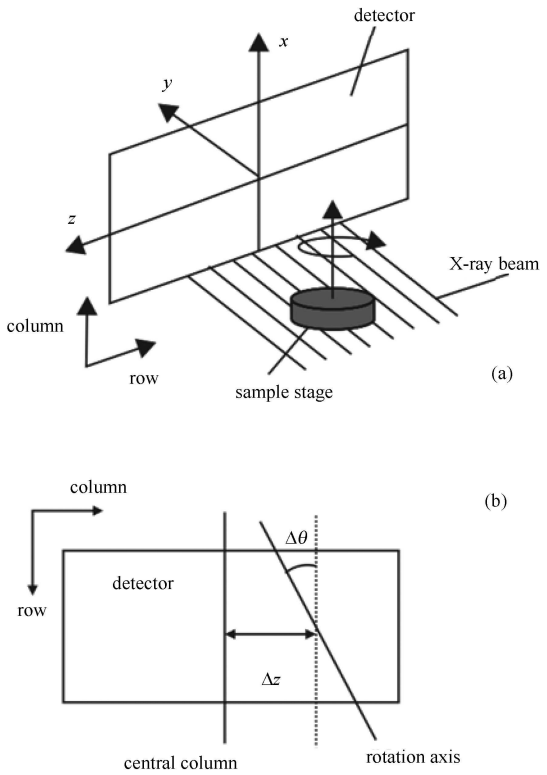

Fig. 3. (a) The ideal parallel-beam CT system; (b) Angle offset and displacement offset.

Normalization correction is the final step to correct for any artificial defects due to illumination changes or variations in detector efficiency and to assure proportionality between the intensity of the reconstructed image (grayscale) and the intensity of incident X-rays. In DEI-CT experiments, the Fourier transform-based reconstruction algorithms assume that stable illumination conditions exists on the CCD scintillator and that each projective image is recorded under such conditions. Unfortunately this is not the case for experimentally acquired data. The unstable electron beam orbits and thermal expansion of the optical elements result in variations in illumination over time. Moreover, in the CCD detector system, detector elements vary in efficiency because of the position of the element in the block, physical variations in the crystal and light guides, and variations in the gains of the photomultiplier tubes. These variations result in substantial high-frequency non-uniformities in the raw data. Thus a normalization correction is needed

to remove these variations in order to meet the requirements for reconstruction algorithms. The procedure mainly does the following. First, after the flat-field and dark field correction and rotation center determination have been carried out, tomography data are converted into a sonogram. Second, some columns in the background of the sinogram are selected which don't contain information about the object, and the averaged values of the selected columns are obtained for each row. Finally, according to the type of tomography data (refraction or absorption information), two formulas (-log (input/ average value), or (input-average value)) are automatically selected for each pixel. Please note that input corresponds to the pixel, which contains information about the object.

Applying the above three corrections to the raw projective images can often ensure data accuracy and remove common image defects to restore the fidelity of the features. These calibrated images can then be input into the tomographic reconstruction, which will be described in the next section.

3 Features of DEI reconstruction

A typical DEI-CT system, as shown in Fig. 4(a)(b), is based on an X-ray source, a monochromator crystal, a rotational sample stage, an analyzer crystal and a detector. When a sample composed of low Z elements is set between the monochromator and the analyzer and illuminated by the X-ray beam, absorption, extinction and refraction occur, so that the intensity measured by the detector after the reflection by the analyzer crystal can be written as [10]:

$$I=I_0\mathrm{e}^{-M(x,y)}\delta(\theta_\mathrm{A}-\theta)\otimes R(\theta_\mathrm{A}), \tag{2}$$

where $M=\int_{-\infty}^{\infty}u(x,y,z)\mathrm{d}t$, μ is the absorption coefficient, I_0 is the intensity of the X-ray beam incident to the sample, $R(\theta)$ is the rocking curve of the DEI-CT system, θ_A is the setting angle of the analyzer, and θ is the refraction angle in the meridianal plane. t is the thickness of the sample.

According to Eq. (2), many different images can be obtained by adjusting the setting angle θ_A of the analyzer to different angles. Among the many possible angles, the two angles $\theta_\mathrm{A}=-\theta_\mathrm{D}/2$ and $\theta_\mathrm{A}=\theta_\mathrm{D}/2$ are those most often used, obtaining two different images identified as the up slope image [6]:

$$I_\mathrm{U}=I_0\mathrm{e}^{-M(x,y)}R\left(-\frac{\theta_\mathrm{D}}{2}\right)[1+C_\mathrm{U}\theta]. \tag{3}$$

And the down slope image

$$I_\mathrm{D}=I_0\mathrm{e}^{-M(x,y)}R\left(\frac{\theta_\mathrm{D}}{2}\right)[1+C_\mathrm{D}\theta]. \tag{4}$$

Here, θ_D is the Darwin width of the rocking curve,

$$C_\mathrm{U}=\frac{1}{R\left(-\frac{\theta_\mathrm{D}}{2}\right)}\frac{\mathrm{d}R\left(-\frac{\theta_\mathrm{D}}{2}\right)}{\mathrm{d}\theta_\mathrm{A}},\ C_\mathrm{D}=\frac{-1}{R\left(\frac{\theta_\mathrm{D}}{2}\right)}\frac{\mathrm{d}R\left(\frac{\theta_\mathrm{D}}{2}\right)}{\mathrm{d}\theta_\mathrm{A}}.$$

Combining the up slope and the down slope images the absorption image and the refraction image can be obtained respectively:

$$I_\mathrm{sum}=I_\mathrm{U}+I_\mathrm{D}, \tag{5}$$

$$\theta=\frac{1}{C_\mathrm{U}}\frac{I_\mathrm{U}-I_\mathrm{D}}{I_\mathrm{U}+I_\mathrm{D}}. \tag{6}$$

The refraction image has a higher contrast and resolution than conventional X-ray projection imaging. However, it is still a 2-D image and all structures inside an object overlap so that it is hard to determine the precise volumetric location of many details inside it. A reliable way to overcome this problem is to combine the DEI method with a CT scan approach to collect real volumetric data, a method that is known as DEI-CT.

Refraction CT based on the DEI set-up

In general the relation between the phase gradient and the refractive index is [11]

$$\frac{\lambda}{2\pi}\frac{\mathrm{d}}{\mathrm{d}s}\nabla\Phi(x,y,z)=\nabla n(x,y,z), \tag{7}$$

where s denotes the position along the path of the X-ray beam. When the X-ray beam goes along the z axis, the beam emerging from the object has a refraction angle given by the integral of all deviations along the path of the beam. Moreover, the phase gradient is small, so the three integrals corresponding to the three components of the gradient of the refractive index are:

$$\theta_x=\int_\mathrm{sample}\frac{\partial n(x,y,z)}{\partial x}\mathrm{d}z, \tag{8}$$

$$\theta_y=\int_\mathrm{sample}\frac{\partial n(x,y,z)}{\partial y}\mathrm{d}z, \tag{9}$$

and

$$\theta_z=\int_\mathrm{sample}\frac{\partial n(x,y,z)}{\partial z}\mathrm{d}z=0, \tag{10}$$

where θ_x and θ_y are the refraction angles in the x-z and the y-z plane, respectively. In Fig. 4(a) and (b), two different DEI-CT setups are shown. Because $\partial n(x,y,z)/\partial y$ is a rotational invariant to reconstruct the slice images, the setup in Fig. 4(a) is based on the conventional algorithm, and the $\partial n(x,y,z)/\partial x$ contribution cannot be collected because of the crystal properties. In contrast, in the second experimental setup, shown in Fig. 4(b), only the $\partial n(x,y,z)/\partial x$ contribution plays the major role in the DEI-CT. But the behavior of $\partial n(x,y,z)/\partial x$ showed in panel (b) is not constant under rotation, which does not satisfy the requirement for CT reconstruction. Therefore, a new CT algorithm based on the layout of Fig. 4(b)

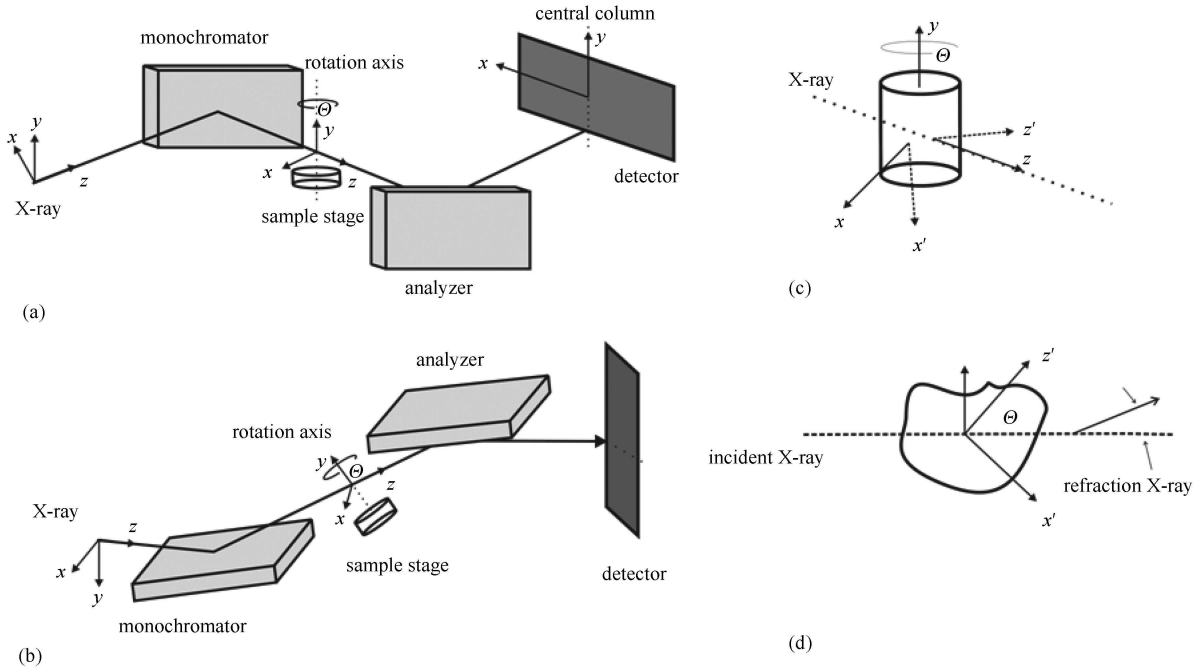

Fig. 4. (a) The rotation axis of the sample is parallel to that of the analyzer; (b) The rotation axis of the sample is perpendicular to that of the analyzer; (c) (x,y,z) and (x',y',z) are associated with the X-ray beam and the sample respectively, Θ is the rotational angle between the two reference frames; (d) Scheme of the refracted X-rays emerging from the sample when the latter is rotated Θ around an axis perpendicular to the paper.

has to be introduced. Looking at Fig. 4(d) and according to Eq. (8) and (10), when an X-ray beam propagates along the z axis, and when the rotation angle of the sample is Θ=0, we may write [12]:

$$\theta_x=\int_{\text{sample}}\frac{\partial n(x,y,z)}{\partial x}\mathrm{d}z=\int_{\text{sample}}|\nabla n|\sin\phi\mathrm{d}z \qquad (11)$$

and

$$0=\int_{\text{sample}}\frac{\partial n(x,y,z)}{\partial z}\mathrm{d}z=\int_{\text{sample}}|\nabla n|\cos\phi\mathrm{d}z. \qquad (12)$$

Combining Eqs. (11) and (12), we obtain

$$\mathrm{i}\theta_x=\int_{\text{sample}}|\nabla n|\exp(\mathrm{i}\phi)\mathrm{d}z. \qquad (13)$$

Looking at the layout of Fig. 4(b), when the sample rotates around the axis perpendicular to the sample stage, $\Theta\neq0$ and a similar equation can be written:

$$\begin{aligned}\mathrm{i}\theta_x^{\Theta}\exp(-\mathrm{i}\Theta) &= \int_{\text{sample}}|\nabla n|\exp(\mathrm{i}\phi)\mathrm{d}z\\ &= \int_{\text{sample}}\left[\frac{\partial n(x',y',z')}{\partial z'}+\mathrm{i}\frac{\partial n(x',y',z')}{\partial x'}\right]\mathrm{d}z,\end{aligned} \qquad (14)$$

in which

$$|\nabla n|\exp(\mathrm{i}\phi)=\frac{\partial n(x',y',z')}{\partial z'}+\mathrm{i}\frac{\partial n(x',y',z')}{\partial x'}$$

is a rotational invariable. Excluding the imaginary term, it is very similar to Eq. (10) in Ref. [13]. Combining Eqs. (2) and (10), we obtain:

$$\begin{aligned}\theta_y^{\Theta}(x,y) &= \left[\frac{\theta_{\mathrm{D}}}{2}\frac{I_{\mathrm{U}}^{\perp}(x,y)-I_{\mathrm{D}}^{\perp}(x,y)}{I_{\mathrm{U}}^{\perp}(x,y)+I_{\mathrm{D}}^{\perp}(x,y)}\right]_{\Theta}\\ &= \int_{\text{sample}}\frac{\partial n(x',y',z')}{\partial y'}\mathrm{d}z.\end{aligned} \qquad (15)$$

Combining Eqs. (6) and (10), we obtain:

$$\begin{aligned}\theta_x^{\Theta}(x,y)\cos\Theta &= \left[\frac{\theta_{\mathrm{D}}}{2}\frac{I_{\mathrm{U}}^{//}(x,y)-I_{\mathrm{D}}^{//}(x,y)}{I_{\mathrm{U}}^{//}(x,y)+I_{\mathrm{D}}^{//}(x,y)}\right]_{\Theta}\cos\Theta\\ &= \int_{\text{sample}}\frac{\partial n(x',y',z')}{\partial x'}\mathrm{d}z,\end{aligned} \qquad (16)$$

$$\begin{aligned}\theta_x^{\Theta}(x,y)\sin\Theta &= \left[\frac{\theta_{\mathrm{D}}}{2}\frac{I_{\mathrm{U}}^{//}(x,y)-I_{\mathrm{D}}^{//}(x,y)}{I_{\mathrm{U}}^{//}(x,y)+I_{\mathrm{D}}^{//}(x,y)}\right]_{\Theta}\sin\Theta\\ &= \int_{\text{sample}}\frac{\partial n(x',y',z')}{\partial z'}\mathrm{d}z,\end{aligned} \qquad (17)$$

where superscripts $\perp$ and // denote the rotation axis of the sample perpendicular or parallel to that of the analyzer, shown in Fig. 4(a)(b).

According to Eqs. (16) (17) and (4) and $C_{\rm U}=-C_{\rm D}$, the low angle images at the rotation angles $\Theta+\pi$ can be rewritten as [14, 15]:

$$[I_{\rm U}(-x,y,z)]_{\Theta+\pi}=[I_{\rm D}(x,y,z)]_{\Theta}. \tag{18}$$

Using this equation, Eqs. (16) and (17) can be rewritten as [7, 8]:

$$\begin{aligned}&\theta_x^{\Theta}(x,y)\cos\Theta\\&=\left\{\frac{1}{C_{\rm L}}\frac{\left[I_{\rm U}^{//}(x,y,z)\right]_{\Theta}-\left[I_{\rm U}^{//}(-x,y,z)\right]_{\Theta+\pi}}{\left[I_{\rm U}^{//}(x,y,z)\right]_{\Theta}+\left[I_{\rm D}^{//}(-x,y,z)\right]_{\Theta+\pi}}\right\}_{\Theta}\cos\Theta\\&=\int_{\rm sample}\frac{\partial n(x',y',z')}{\partial x'}{\rm d}z,\end{aligned} \tag{19}$$

$$\begin{aligned}&\theta_x^{\Theta}(x,y)\sin\Theta\\&=\left\{\frac{1}{C_{\rm L}}\frac{\left[I_{\rm U}^{//}(x,y,z)\right]_{\Theta}-\left[I_{\rm U}^{//}(-x,y,z)\right]_{\Theta+\pi}}{\left[I_{\rm U}^{//}(x,y,z)\right]_{\Theta}+\left[I_{\rm U}^{//}(-x,y,z)\right]_{\Theta+\pi}}\right\}_{\Theta}\sin\Theta\\&=\int_{\rm sample}\frac{\partial n(x',y',z')}{\partial z'}{\rm d}z.\end{aligned} \tag{20}$$

Equations (19) and (20) can be used with the conventional algorithm to reconstruct three dimensional images of the gradient of the refractive index. The reconstruction algorithm formula is [16]:

$$\begin{aligned}\frac{\partial n(x',y',z')}{\partial x'}&=\int_0^{\pi}{\rm d}\Theta\int_{-\infty}^{\infty}\left[\theta_x^{\Theta}(x,\Theta,y)\cos\Theta\right]*F^{-1}\{|\rho|\}\\&\quad\times\delta(x'\cos\Theta+z'\sin\Theta-x){\rm d}x,\end{aligned} \tag{21}$$

$$\begin{aligned}\frac{\partial n(x',y',z')}{\partial z'}&=\int_0^{\pi}{\rm d}\Theta\int_{-\infty}^{\infty}\left[\theta_x^{\Theta}(x,\Theta,y)\sin\Theta\right]*F^{-1}\{|\rho|\}\\&\quad\times\delta(x'\cos\Theta+z'\sin\Theta-x){\rm d}x,\end{aligned} \tag{22}$$

$$\begin{aligned}\frac{\partial n(x',y',z')}{\partial y'}&=\int_0^{\pi}{\rm d}\Theta\int_{-\infty}^{\infty}\left[\theta_y^{\Theta}(x,\Theta,y)\right]*F^{-1}\{|\rho|\}\\&\quad\times\delta(x'\cos\Theta+z'\sin\Theta-x){\rm d}x.\end{aligned} \tag{23}$$

Using Eqs. (19) and (21), the algorithm formula to reconstruct the refractive index can be written as [17]:

$$\begin{aligned}n(x',y',z')&=\int_0^{\pi}{\rm d}\varphi\int_{-\infty}^{\infty}\left[\theta_x(x,\Theta,y)*F^{-1}\left(\frac{|\rho|}{2\pi{\rm j}\rho}\right)\right]\\&\quad\times\delta(x'\cos\varphi+z'\sin\varphi-x){\rm d}x.\end{aligned} \tag{24}$$

Figure 1 shows the GUI for DEI reconstruction. Using the method menu, a user can select the reconstruction algorithm for refraction CT or DPI-CT, respectively. Based on the two different optical layouts shown in Fig. 4(a) and (b), two sets of test data, shown in Fig. 5(a)(b), were collected to test the reconstruction algorithm for refraction CT. The test sample was a quarter of a simple epoxy cylinder containing a few air bubbles of different sizes. Fig. 5(b) and (c) are the 108th slice images of $\partial n/\partial x$,$\partial n/\partial y$, the air bubble can be seen clearly. Fig. 5(c) is the 280th reconstructed slice image of $\partial n/\partial z$; some of the circles shown in Fig. 5(c) are lighter and the others are darker. This is because a spherical bubble can be divided into two symmetrical parts and these two parts refract the X-ray in opposite directions, and so we obtain the white and black circles shown in Fig. 5(c). Fig. 5(e) is the 280th reconstructed slice image of n. All the reconstructed slice images shown in Fig. 5 agree with the results in Refs. [16, 18], which demonstrate the accuracy and effectiveness of the DEI reconstruction program.

4 Features of DEI information extraction

As described by Eq. (2), the two images obtained using the analyzer set to the sides of the rocking curve are observed to contain a mixture of refraction and absorption. These two images were arithmetically combined to obtain a refraction angle image with the refraction angle measured in the diffraction plane of the DEI system. An absorption image was also obtained. However, due to

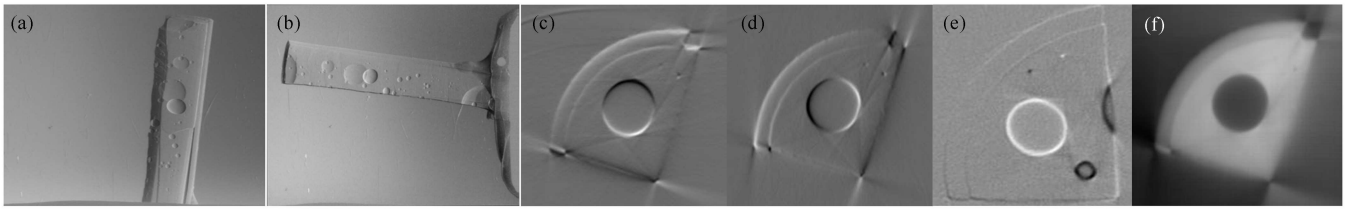

Fig. 5. Refraction CT data and the reconstructed slice images. (a) (b) two different projective images of the test sample; (c) the reconstructed slice image of $\partial n/\partial x$; (d) the reconstructed slice image of $\partial n/\partial y$; (e) the reconstructed slice image of $\partial n/\partial z$; (f) the reconstructed slice image of n.

the limited information contained in the images, it was not possible to use the previous DEI method described by Eq. (2) to determine scattering information, because Eq. (2) neglects the contribution of small angle scattering. Therefore, a more accurate DEI method is needed to determine the extinction, refraction, absorption and small angle scattering properties of the object from the measured intensities.

A simpler and more effective method is the multiple-images statistical (MIS) method, which makes several image measurements of the object at various settings of the analyzer crystal in relation to the rocking curve. To apply this method, a model of the object's absorption, refraction angle and extinction has been developed. To simplify the model, a Gaussian angular distribution and single scattering theory were used. This model simulates the rocking curve observed in a detector pixel through the object with the DEI system [19]:

$$I = I_0 \mathrm{e}^{-M} \int_{-\infty}^{+\infty} \left\{ \mathrm{e}^{-\Gamma} \delta(\theta-\theta_x) + \frac{1}{\sqrt{2\pi}\sigma}(1-\mathrm{e}^{-\Gamma})\mathrm{e}^{-(\theta-\theta_x)^2/2\sigma^2} \right\} * R_{\mathrm{int}}(\theta-\theta_x)\mathrm{d}\theta. \quad (25)$$

Where $\Gamma = \int_{-\infty}^{\infty} \chi \mathrm{d}t$, $\sigma = \int_{-\infty}^{\infty} \omega_{\mathrm{s}} \mathrm{d}t$, χ is the extinction coefficient, ω_{s} is the Gaussian width of scatter distribution. $R_{\mathrm{int}}(\theta)$ is the intrinsic rocking curve, which is the reflectivity profile obtained in the absence of the object. This equation has two parts. The first part is the direct beam, which experiences intensity loss from absorption and extinction, and the second part is the scattered beam. The first portion after integration has a width given by the DEI system rocking curve. The second part, by the same token, has a width determined by the convolution of the ultra-small angle scattering distribution of the object with the DEI system. Also, it should be noted that this model has the following normalized value when integrated over all the settings of the analyzer:

$$\Omega = \int I(\theta_{\mathrm{A}})/I_0 \mathrm{d}\theta_{\mathrm{A}} = \omega_{\mathrm{int}} \mathrm{e}^{-M}. \quad (26)$$

Where ω_{int} is the integral of $R_{\mathrm{int}}(\theta)$, when there is no object present then the integrated reflectivity is simply ω_{int}. Therefore, Eq. (26) suggests that the scattered intensity is not really lost but only scattered away and can be recovered by integrating Eq. (25) or by integrating the observed intensity profile. Thus, this model has the properties we expect from an object that refracts, absorbs, and scatters X-rays. Using this model, the MIS method can obtain the refraction angle θ_x from the centroid of the sample rocking curve obtained at each point in the image. Moreover, integrating the rocking curve obtained at each pixel and normalizing this integral by the intrinsic rocking curve determines the absorption image according to [19]:

$$M = -\ln\left(\frac{\Omega}{\omega_{\mathrm{int}}}\right). \quad (27)$$

After M has been found, the estimate of the extinction image Γ is obtained by assuming the maximum measured photon count as the rocking curve is affected by only absorption and extinction according to [19]:

$$\Gamma = -\ln(I_{\mathrm{peak}}/I_0) + M. \quad (28)$$

An initial estimate of the scattering width σ, was obtained from the Darwin width (θ_{D}) of the intrinsic rocking curve and the measured FWHM (σ_{R}) at the pixel location, according to:

$$\sigma = \sqrt{\sigma_{\mathrm{R}}^2 - \theta_{\mathrm{D}}^2}. \quad (29)$$

Because Eq. (28) resembles Beer's law, the extinction image Γ can be reconstructed with the conventional CT algorithm based on the Radon transformation, which is diffraction peak imaging CT (DPI-CT).

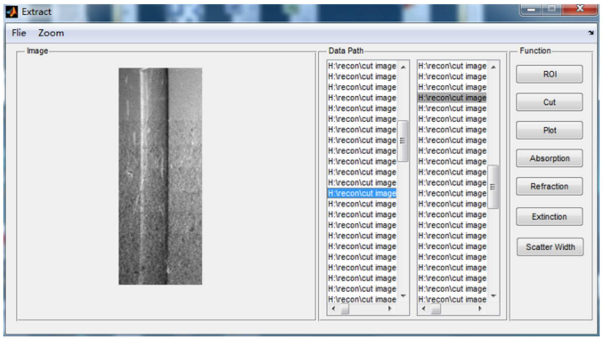

(a)

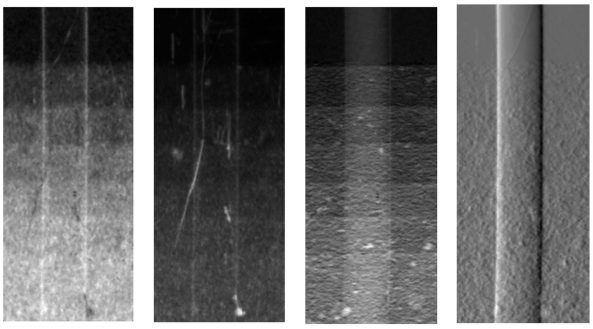

(b) (c) (d) (e)

Fig. 6. The DEI information Extraction GUI with test data (a sample composed of paper and a cylindrical Lucite rod). (b) shows the extinction image Γ, (c) the scattering width image σ, (d) the absorption image M, and (e) the refraction angle image θ_x.

A screen shot of the GUI for the DEI information Extraction is shown in Fig. 6. A test dataset of a 0.5 mm diameter Lucite rod overlaid by paper layers (0–7 layers) demonstrates the capability of this program. As shown in Fig. 6(b), it is clear that with an increasing number of paper layers, the extinction increases. The intensity changes as a step function from one layer to the next, which proves that the algorithm described by equation (28) isolates the refraction and absorption effects from extinction. Fig. 6(c) is the scattering width image σ, which is similar to the extinction image shown in Fig. 6(b). Fig. 6(d) and Fig. 6(e) are the absorption image M and refraction angle image θ_x, respectively. Because of the shape of the Lucite rod, positive and negative contrasts are observed in Fig. 6(e). This implies that the refracted beam changes direction.

5 Conclusion

The DEIReconstructor software has been developed to fulfill the demands of modern DEI experiments. It integrates mathematical and visualization capabilities to support imaging pre-processing, extract the absorption, refractive and scattering information from diffraction enhanced imaging, and allows for parallel-beam tomography reconstruction for DEI-CT. The DEIReconstructor GUI has been carefully constructed to be easy to use and is a powerful tool for visualization of the internal structure of low-Z samples. Future developments of the software will focus on speed improvement (algorithms, higher degree of parallelization). The code can be provided by the author (zhangk@ihep.ac.cn).

References

1 Dilmanian F et al. Phys. Med. Biol., 2000, **45**: 933
2 Wilkins S et al. Nature, 1996, **384**: 335
3 Chapman D et al. Synchrotron Radiation News, 1998, **11**: 4
4 Momose A, Kawamoto S. Jpn. J. Appl. Phys., 2006, **45**: 314
5 Pavlov K et al. J. Phys. D: Appl. Phys., 2001, **34**: 168
6 ZHU P et al. J. Phys. D: Appl. Phys., 2006, **39**: 4142
7 ZHU P et al. PNAS, 2010, **107**: 13576
8 ZHANG K et al. Phys. Med. Biol., 2008, **53**: 5757
9 CHEN R C et al. J. Synchrotron. Radiat, 2012, **19**: 836
10 Chapman D et al. Phys. Med. Biol., 1997, **42**: 2015
11 ZHANG K et al. Anal. Bioanal. Chem., 2010, **397**: 2067
12 ZHU P P et al. Appl. Phys. Lett., 2005, **87**: 264101
13 Maksimenko A et al. Appl. Phys. Lett., 2005. **86**: 1241051
14 ZHANG X et al. Phys. Med. Biol., 2008, **53**: 5735
15 WANG M et al. J. Phys. D: Appl. Phys., 2007, **40**: 6917
16 WANG J et al. Phys. Med. Biol., 2006, **51**: 3391
17 HUANG Z et al. Appl. Phys. Lett., 2006, **89**: 041124
18 SUN Y et al. Computerized Tomography Based on X-ray Refraction Information. In Biomedical Imaging: Nano to Macro, 2006. 3rd IEEE International Symposium on. 2006. 1022
19 Oltulu O et al. J. Phys. D: Appl. Phys., 2003, **17**: 2152